Construction of a thermodynamic potential for the water ices VII and X

Martin French and Ronald Redmer

Institut für Physik, Universität Rostock, D-18051 Rostock, Germany

We employ a combination of density functional theory (DFT), molecular dynamics (MD), and a variety of advanced postprocessing methods to construct an analytic thermodynamic potential (free energy) for ices VII and X. In particular, the temperature-dependent part of the free energy function is constructed using entropy data obtained via the spectrum of vibrational modes from the MD simulations. Conceptional challenges due to the partial absence of stable zero-temperature states and proton disorder are overcome by performing calculations of representative crystalline states combined with a three-stage fitting procedure of data from MD simulations and static DFT calculations. The influence of the exchange-correlation functional is extensively discussed, and a comparison with available experiments is made as well and generally shows good agreement. This work is of significant importance for astrophysical applications, such as the interior modeling of dense icy planets and moons.

I. INTRODUCTION

The phase diagram of water is rich in transitions between various solid structures, most of which are composed of H_2O molecules in different arrangements. A particularly interesting part of this phase diagram is the high-pressure ices for which the nature of the interactions changes from a hydrogen-bonded molecular solid to an ionic crystal. This occurs in the region of ices VII and X, which exist under pressures between 2 GPa and several hundred gigapascals and temperatures between a few hundred degrees Kelvin to 2000 K [1]. Such states are present, e.g., in icy planetary objects like cold super-Earths or ice giants in their later evolution stages [2,3].

Structural and thermodynamic properties of both ices VII and X were extensively probed with optical, x-ray, and neutron scattering methods using diamond-anvil cells [4–29]. They were also the subject of numerous theoretical investigations [30–38], but no serious attempt has yet been made to develop a complete equation of state (EOS) on the level of a thermodynamic potential for both ices VII and X.

Ices VII and X share the same crystalline bcc oxygen structure, but their electronic and protonic bonding mechanisms are fundamentally different. Ice VII consists of molecules bound via hydrogen bonds that form a proton-disordered structure [1]. The protons are located on off-center positions on the space diagonal of the bcc cell [39] (see Fig. 1). Under compression or heating, the protons can cross a potential barrier midway along the space diagonals on short time scales and can form a dynamically disordered ice VII [34] (labeled here as ice VII*). At very high density the protons are forced to occupy symmetric positions between the oxygen nuclei, which results in the formation of an ionic crystal of cuprite structure: ice X.

The aim of this work is to construct a smooth function for the free energy $f(\varrho,T)$ that reflects the general behavior of the EOS, such as pressure $p(\varrho,T)$, internal energy $u(\varrho,T)$, and entropy $s(\varrho,T)$, of ices VII, VII*, and X with high accuracy. We do not attempt to accurately classify the order or the exact location of the intricate transitions between the ices. The nature of these phase transitions is an extensively debated subject in the literature [12,18,19,23,27,38], and their locations are not exactly known throughout the pressure-temperature plane

either. Most likely, these transitions are continuous, and thus, they leave only very subtle signatures in the EOS.

The methods to achieve the goal are based on density functional theory (DFT), combined mostly with molecular dynamics (MD) simulations and, to a lesser extent, with phonon calculations. A variety of postprocessing techniques are employed as well. Details are described in the following sections.

The EOS derived in the present work is valid in the entire stability region of ices VII, VII*, and X and is well behaved in extrapolation. It can be used by itself in the analytical form presented here but is intended to become part of a wide-range tabular EOS of water to be constructed in the future.

II. DESCRIPTION OF THE METHODS

The principal method used here is performing electronic structure calculations with density functional theory [40–42] using the Vienna Ab Initio Simulation Package (VASP). [43–45] These DFT calculations are performed either for fixed configurations of protons and oxygen nuclei or in combination with classical molecular dynamics (MD) simulations. In all cases, periodic boundary conditions are imposed, and the electronic wave functions are expanded in plane waves, importantly, using projector-augmented-wave (PAW) pseudopotentials [46,47] provided with VASP.

The choice of the exchange-correlation (XC) functional is a very critical aspect in DFT calculations. Here we mainly use the XC functional of Perdew, Burke, and Ernzerhof (PBE) [48]. A comparison with other XC functionals is made as well, and the implications are discussed in detail in the following sections.

A. Details of the DFT calculations

Three main types of DFT calculations are used: static calculations with small unit cells for ideal lattice energies, static calculations with large unit cells including nuclear displacements to calculate phonons, and DFT-MD for direct calculations of thermodynamic quantities. Details are as follows.
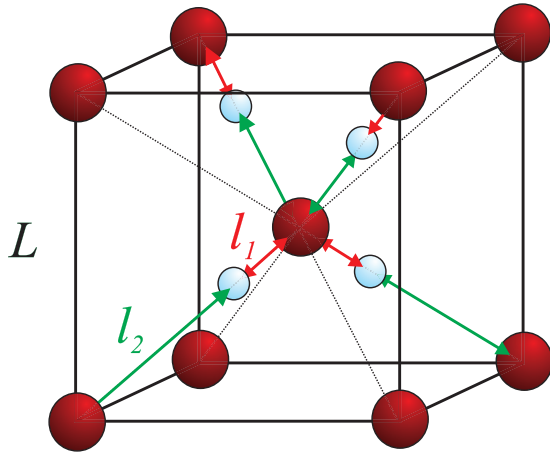
FIG. 1. (Color online) Idealized [39] proton-ordered unit cell of ices VII and X, where the lattice constant is labeled L. The lengths l_1 and l_2 indicate the two smallest possible distances of the protons (small spheres) to oxygen nuclei (large spheres), where $l_2 \geqslant l_1$ and $l_1 + l_2 = \sqrt{3}L/2$.

Several static DFT calculations are made with a single unit cell containing four protons and two oxygen nuclei to calculate electronic ground-state energies. For ice X additional calculations with supercells containing 256 protons and 128 oxygen nuclei are made to determine forces which are then used in phonon calculations [49,50] with the PHONOPY [51] code. These forces are obtained by displacing selected nuclei by small finite differences from their ideal lattice positions. The subsequent phonon calculations then yield the dispersion relation of the phonon frequencies, from which the contribution of the nuclear motion to the thermodynamic properties is calculated in the quasiharmonic approximation. For the crystalline phase ice X, this would be sufficient to determine a well-founded EOS for not too high temperatures. However, phonon calculations are not possible for ices VII and VII* because they do not possess dynamically stable ground states. Apart from that, anharmonic effects also need to be included in an appropriate way for ice X at high temperatures.

The majority of our DFT calculations are thus made within DFT-MD simulations. There the classical nuclei are propagated with forces derived from the DFT calculations for each nuclear configuration. After equilibration, the statistically averaged values for the internal energy and pressure can be calculated easily. Such a dynamic approach is necessary for a satisfactory description of the microscopic mechanisms of nuclear motion in ices VII and VII*. The DFT-MD simulations are performed using the Nosé thermostat [52] to control the temperature.

Achieving good numerical convergence of all physical quantities calculated with DFT-MD is of utmost importance and must be ensured [53]. Since we extensively applied the same DFT-MD simulation technique in previous work on water [54–60], we can rely, to a large extent, on the extensive numerical testing that was done there. For example, the validity of the standard PAW pseudopotentials for hydrogen and oxygen under the conditions of interest was shown [54]. A cutoff energy of 900 eV is also known to yield well-converged

forces and thermodynamic quantities such as internal energy and pressure.

In the DFT-MD simulations of the present work we use a standard time step of 0.4 fs, but each simulation is run for about 10 000 to 40 000 time steps. Such long simulations are required to calculate frequency spectra from velocity autocorrelation functions (see the next section), which we heavily rely on in this work, with sufficient accuracy. Different **k**-point sets are chosen depending on the particle numbers; for example, the Γ point was used for all MD simulations which were made with 54 molecules.

For the static DFT calculations with two molecules a $6 \times 6 \times 6$ Monkhorst-Pack **k**-point set [61] was used. The calculations of the forces for the phonon dispersion in ice X were made with 128 molecules and $2 \times 2 \times 2$ **k** points to achieve the best convergence of the respective thermodynamic properties obtained within this kind of approximation.

B. Postprocessing using frequency spectra

Thermodynamic quantities obtained with a purely classical description of the ionic motion are inadequate to construct a valid EOS for the ices. One fundamental problem is that the entropy diverges logarithmically at $T = 0$ for a classical system, e.g., for the harmonic oscillators present in our MD simulations of the ices at low temperature. Furthermore, the heat capacity would be drastically overestimated because typical vibrational temperatures of a water molecule (or phonon frequencies in ice) amount to several thousand degrees Kelvin, thus exceeding even the melting temperature of the ices.

Ideally, one would aim to perform path-integral MD simulations [33] or to use a semiclassical thermostat [38] as a solution, but a powerful remedy for this problem is also available within the classical MD scheme. It involves the calculation of the following spectrum of the vibrational modes (power spectrum) in the MD [62]:

$$S(\nu, \varrho, T) = \sum_\alpha \frac{4 m_\alpha N_\alpha}{3 N k_B T} \int_0^\infty dt \cos{(2\pi \nu t)} \langle \vec{v}_\alpha(t) \cdot \vec{v}_\alpha(0) \rangle, \tag{1}$$

where k_B is Boltzmann's constant and m_α is the mass of a nucleus of species α. The total number of nuclei N is given by the sum of the number of nuclei N_α of each species. The centerpiece in expression (1) is the Fourier transformation of the velocity autocorrelation functions $\langle \vec{v}_\alpha(t) \cdot \vec{v}_\alpha(0) \rangle$ of each ion species. The spectrum $S(\nu, \varrho, T)$ formally fulfills the normalization condition

$$\int_0^\infty d\nu \, S(\nu, \varrho, T) = 1, \tag{2}$$

which is, in practice, achieved with an accuracy of 1% or better. The spectrum implicitly contains anharmonic effects from the DFT-MD simulations.

Having calculated such a spectrum for a DFT-MD simulation, one obtains a correction term for the internal energy that replaces the classical energy of a harmonic oscillator mode $k_B T$ with its quantum statistical value for each frequency

interval in the following way [62]:

$$u_{vc}(\varrho,T) = \frac{3N}{m} \int_0^\infty d\nu \, S(\nu,\varrho,T)$$
$$\times \left[h\nu \left(\frac{1}{2} + \frac{1}{\exp(h\nu/k_B T) - 1} \right) - k_B T \right], \quad (3)$$

where $m = \sum_\alpha N_\alpha m_\alpha$ is the total mass of all nuclei. This correction value is then added to the standard internal energy $u_{MD}(\varrho,T)$ of each DFT-MD simulation. The capability of this approach was examined in application to various phases of ammonia [63] and, in a simpler version, also to fluid water [55]. Significantly improved Hugoniot temperatures were calculated in both cases. For methane it was reported that the results are of the same quality as those directly obtained with a semiclassical thermostat [64].

Moreover, one can calculate the thermal contribution to the nuclear entropy in a related way [62]:

$$s_{\text{vib}}(\varrho,T) = \frac{3N}{m} \int_0^\infty d\nu \, S(\nu,\varrho,T) k_B \left\{ \frac{h\nu/k_B T}{\exp(h\nu/k_B T) - 1} \right.$$
$$\left. - \ln[1 - \exp(-h\nu/k_B T)] \right\}. \quad (4)$$

This expression contains the quantum-statistical entropy weighting function of a harmonic oscillator under the integral. Equation (4) can be evaluated without difficulty as long as there is no zero-frequency component in the spectrum $S(\nu,\varrho,T)$. This is fulfilled when the material is solid; that is, no diffusive nuclear motion occurs.

We note that the approach is approximate and has some limitations, and we discuss these aspects qualitatively in the Appendix. However, we did not observe this method to introduce any major source of error into our thermodynamic data, especially compared to several other approximations made in this work.

III. STRUCTURAL AND THERMODYNAMIC ANALYSIS OF THE DFT-MD SIMULATIONS

We restrict our analysis to ice phases VII, VII*, and X. A total number of 92 MD simulations of these ices were made on a largely regular grid in the density-temperature plane. The densities were varied between 1.6 and 4.25 g/cm^3, and the temperatures were chosen from 295 up to 2000 K. Additional simulation runs at 2250 K and higher temperatures resulted in either molten or superionic structures [54,65], which were identified using a mean-square displacement analysis of diffusion and were not considered any further. Densities of 4.5 g/cm^3 and higher lead to a distortion of the bcc oxygen lattice, which is induced by a dynamic instability that indicates a transition to a different ice with orthorhombic crystal structure [36,66].

The pressure $p_{MD}(\varrho,T)$ and the internal energy $u_{MD}(\varrho,T)$ from the MD simulations do not show any sign of a discontinuity [67] throughout the density-temperature plane. This observation motivates us to attempt the construction of a continuous thermodynamic potential that describes all three ices of interest with a smooth function. The behavior of both $p_{MD}(\varrho,T)$ and $u_{MD}(\varrho,T)$ is unspectacular, and we do not
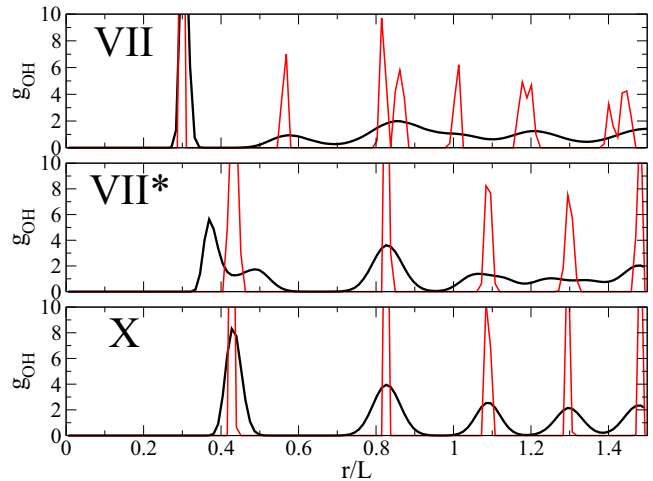

FIG. 2. (Color online) Oxygen-proton pair-correlation functions of ice VII at 1.75 g/cm^3 (upper panel), ice VII* at 2.75 g/cm^3 (center panel), and ice X at 3.75 g/cm^3 (lower panel). The temperature was 400 K in all cases. Standard pair-correlation functions $g_{OH}(r)$ from the MD simulations are shown in black. The special pair-correlation functions $\bar{g}_{OH}(r)$ calculated from the time-averaged nuclear coordinates are drawn in red.

display these quantities here. Corresponding data have already been published in Ref. [54]. In fact, we do not even use the pressures $p_{MD}(\varrho,T)$ at all during the course of this work.

A. Identification of the ice phases

In order to distinguish between the ice VII, ice VII*, and ice X structures formed in the MD simulations, it is sufficient to examine radial oxygen-proton pair-correlation functions, and we do so in the following way: in addition to the standard pair-correlation functions $g_{OH}(r)$, we also compute special pair-correlation functions $\bar{g}_{OH}(r)$ from the nuclear coordinates averaged over the entire simulation run. Representative results of these pair-correlation functions are plotted in Fig. 2. The position coordinate r is normalized to the lattice constant L for easier interpretation.

In the MD simulations of ice VII the protons do not jump along the space diagonal. Therefore, the first two peaks in $g_{OH}(r)$ are well separated from each other. The corresponding function $\bar{g}_{OH}(r)$ shows narrow peaks that correspond to nuclear distances in the ideal crystal structure initialized at the beginning of a simulation. In the dynamically disordered ice VII*, the protons hop frequently between two equivalent positions along the space diagonal. This results in a merging of the first two peaks in $g_{OH}(r)$. In addition, the protons occupy the same central location between the oxygen nuclei, on average, that they hold in ice X. The first peak in $\bar{g}_{OH}(r)$ is thus located at $r/L = \sqrt{3}/4$. For ice X $g_{OH}(r)$ displays the symmetric proton distribution generated by relatively harmonic vibrations around the ideal lattice sites of the protons in the cuprite structure.

When plotting the ratio of the positions of the first two peaks at l_1 and l_2 in $g_{OH}(r)$ versus the density for ices VII and VII*, one obtains a set of data points that can be fitted very

well to the linear function

$$\frac{l_2}{l_1} = 2.77 - 0.53\varrho, \tag{5}$$

where ϱ is to be entered in g/cm^3. The above expression describes the decrease of the asymmetry parameter l_2/l_1 in ices VII and VII*. The transition to ice X is located where $l_2/l_1 = 1$ is fulfilled, i.e., at a density of 3.34 g/cm^3. However, even at substantially lower densities, e.g., at 3.25 g/cm^3, both first peaks in $g_{OH}(r)$ may be virtually indistinguishable, and even the asymmetry in this peak can be small. A rigorous determination of a sharp transition between ices VII* and X is thus extremely difficult to infer from such structural analyses in real space, especially at high temperatures. However, we are not required to achieve this for our purposes because all the simulation data of the ices VII* and X are processed in the same way.

We also point out that a sound atomistic distinction between the ice VII and VII* phases is only possible when treating all nuclei as purely classical particles and at $T = 0$. In a quantum-mechanical description there should always be a finite probability for the protons to dynamically cross the double-well potential barrier. The same applies when thermal fluctuations are present. The question is merely if the time scales during which atomistic simulations or experiments are made allow one to actually observe such events.

B. Structural influence on the nuclear quantum effects

A particularly insightful picture is acquired when combining information about the phase with the calculated quantum correction to the internal energy $u_{vc}(\varrho,T)$ (see Fig. 3).

It is natural that the magnitude of this quantum correction decreases systematically with the temperature for all ice phases. By definition, $u_{vc}(\varrho,T)$ increases as the vibrational

FIG. 3. (Color online) Quantum correction term $u_{vc}(\varrho,T)$ as obtained from Eq. (3). The open circles represent ice VII, the solid circles indicate ice VII*, and the squares show ice X. Small diamonds with colors identical to those of the large symbols (circles and squares) show the residual internal energy data used to fit the nuclear ground-state energy in Sec. IV C. The black line is the respective fit from Eq. (15).

frequencies in the ices become higher. Therefore, the density dependence is strongly influenced by the phase of the ice.

In ice VII $u_{vc}(\varrho,T)$ is almost constant, perhaps slightly increasing with the density. A small increase with the density is expected because this reflects a common shift to higher vibrational frequencies with increasing density (phonon hardening) [49].

In the dynamically disordered ice VII* a noticeable decrease occurs, which can be understood by the gradual transformation of the fast OH stretch mode in the molecular ice VII into an effective low-frequency mode assigned to the hopping motion of a proton along the space diagonal. The probability of such proton jumps increases with the density as the potential hill between the minima in the double-well potential is lowered. In the vicinity of ice X, the decrease in $u_{vc}(\varrho,T)$ gets weaker since the distance between the minima gets shorter, which leads to shorter times the proton needs to cover it. The inversion to the normal effect of phonon hardening in ice X occurs close to where the transition between ice VII* and ice X is estimated from the pair-correlation functions, as described in the previous section.

All in all, each of the phases show their own characteristic influence on $u_{vc}(\varrho,T)$, but there is no sign of a discontinuity at any transition.

IV. CONSTRUCTION OF THE FREE ENERGY

For convenience we decompose our free energy $f(\varrho,T)$ into three parts which we label as the electronic ground-state energy $u_e(\varrho)$, nuclear ground-state energy $u_n(\varrho)$, and a thermal contribution $f_t(\varrho,T)$. These individual parts do not necessarily have the physical meaning of what they are labeled as, which will become clear in the descriptions that follow. They act only as a representation of such, as if we were treating a single crystalline phase with a well-defined thermodynamic ground state [49]. Only the full expression,

$$f(\varrho,T) = u_e(\varrho) + u_n(\varrho) + f_t(\varrho,T), \tag{6}$$

contains the physically relevant information in the end. In this representation, the free energy is a thermodynamic potential, so that all other thermodynamic quantities can be calculated, e.g., by analytical differentiation. For instance, we can obtain the pressure

$$p(\varrho,T) = \varrho^2 \left(\frac{\partial f}{\partial \varrho} \right)_T \tag{7}$$

or the internal energy

$$u(\varrho,T) = -T^2 \left(\frac{\partial (f/T)}{\partial T} \right)_\varrho. \tag{8}$$

The following sections focus on each of the individual terms in Eq. (6). They also include discussions about the influence of the XC functional used in the DFT. A final consistency check against the internal energy from the MD simulations is also presented.

A. Electronic ground-state energy

This part is calculated by performing static DFT calculations with one idealized unit cell, as displayed in Fig. 1. The
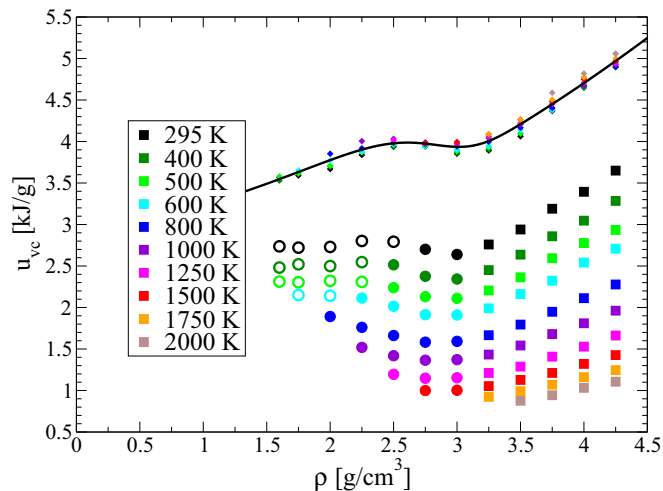
TABLE I. Coefficients used in Eq. (9). All units are chosen in a way that entering the density in g/cm^3 leads to results for u_e in kJ/g.

	PBE	HSE	vdW-optB86b	AM05	LDA
a_0	78.0913	−16.8923	84.7263	137.924	134.099
a_1	−172.712	−85.0197	−175.063	−217.067	−240.338
a_2	18.095	8.33865	18.6251	22.4402	25.5167
a_3	−0.717051	−0.150425	−0.757606	−0.943835	−1.13834
a_4	130.541	59.9442	131.406	166.409	182.303
a_5	67.2915	38.2224	66.7509	82.6152	88.3112

asymmetry parameter l_2/l_1 in the proton distribution in ices VII and VII* depends on the density, and it is determined from Eq. (5). Note that this structure does not correspond to a proton-disordered structure but to a closely related artificial crystal instead. The energy curve generated this way is very consistent with the internal energies calculated from the MD simulations at nonzero temperature and serves us well for our EOS construction purposes. For densities at which the ratio l_2/l_1 decreases to 1 or less, the ice X crystal structure is used.

In addition to the calculations with the PBE functional, we have also made corresponding DFT calculations with the local-density approximation (LDA) [68,69], the AM05 [70], the hybrid HSE [71,72] (using 25% Hartree-Fock exchange and a screening parameter of $\mu_s = 0.2$ Å^{-1}), and the van der Waals–optB86b [73] XC functionals. The latter was shown to be capable of reaching a high accuracy for predictions of lattice constants and bulk moduli that is comparable to quantum Monte Carlo results [74].

We fit the internal energy from these DFT calculations to the following functional form:

$$u_e(\varrho) = a_0 + a_1\varrho + a_2\varrho^2 + a_3\varrho^3 + a_4 \ln \varrho + a_5 (\ln \varrho)^2 . \quad (9)$$

Such a combination of polynomials of the density and its logarithm allows excellent fits to the DFT results, i.e., with correlation coefficients of ≈ 0.99999 for each set of 21 data points between 1 and 5 g/cm^3. The coefficients are given in Table I.

The XC functional significantly influences the results for u_e in a similar way, as is well known for many crystalline substances [73,75–78]. The quantitative effect is best illustrated by calculating the respective pressures $p_e(\varrho) = \varrho^2(\partial u_e/\partial \varrho)$, which are shown in Fig. 4. The deviations between the curves are systematic. The PBE XC functional produces the highest pressure, and LDA produces the lowest pressure, while the results from other XC functionals lie somewhere in between. The difference between PBE and vdW-optB86b is relatively small, e.g., 3 GPa at a density of 4 g/cm^3, while it surmounts 15 GPa between PBE and LDA. Interestingly, both the AM05 and the HSE hybrid functionals show a bridging-like behavior between the vdW-optB86b XC functional at low density and the LDA at high density. In doing so, HSE coincides with PBE in an intermediate density range.

To achieve consistency with the MD simulations, we will use the results using the PBE functional throughout the construction procedure for the thermodynamic potential. Having explored the general influence of the XC functional on the electronic ground-state energy, we will not make a final
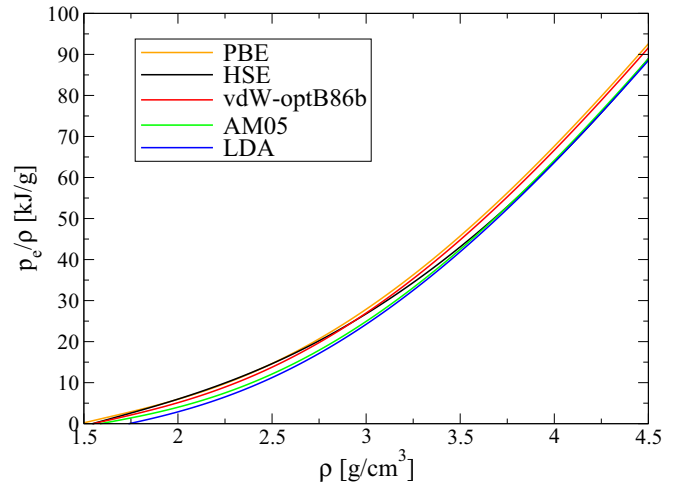

FIG. 4. (Color online) Reduced pressures $p_e(\varrho)/\varrho$ for different XC functionals.

recommendation on which one is the best to use until after Sec. V, where a comparison with experiments is made.

B. The thermal contribution

The temperature-dependent term $f_t(\varrho,T)$ is constructed using the entropy derived from the DFT-MD simulations and phonon calculations. It is mainly determined by the thermal motion of the nuclei, and the respective quantity $s_{\mathrm{vib}}(\varrho,T)$ is calculated via Eq. (4). Electronic excitations, which are also accessible within the finite-temperature formulation of DFT used here [42], do not play any role.

Importantly, there is an additional structural contribution to the entropy in ice VII due to the proton disorder [1,79]. It amounts (in very good approximation) to

$$s_p = \frac{R}{M} \ln \frac{3}{2} \approx 0.135 k_B/\mathrm{atom}, \quad (10)$$

where R is the ideal gas constant and $M = 18.0$ g/mol is the molar mass of molecular water. Such structural entropy cannot be calculated directly with the MD simulations of ice VII. To circumvent any possible ambiguities, we always initialize the proton-ordered crystal structure from Fig. 1 in the MD simulations for ice VII, so that s_p can be added afterward to $s_{\mathrm{vib}}(\varrho,T)$ but only in the case of ice VII.

In ice VII* the proton disorder is achieved dynamically in the simulations, and its corresponding entropy is directly captured in $s_{\mathrm{vib}}(\varrho,T)$ via the partial low-frequency mode associated with the hopping motion in the spectrum, similar to what was discussed in Sec. III B. The functional form of the weighting function for the entropy in Eq. (4) causes the entropy to increase as the frequencies in $S(\nu,\varrho,T)$ decrease. In ice X there is no structural disorder, so that term is irrelevant there.

In addition, the occurrence of structural entropy due to static proton disorder in ice VII can theoretically be understood within the dynamic approach as well. It is formally achieved by the simultaneous compensation of a diverging entropy weighting function and an infinitely small frequency mode in $S(\nu)$ at $\nu = 0$. In the limit of infinitely slow hopping motion, both the frequency and the magnitude of its corresponding
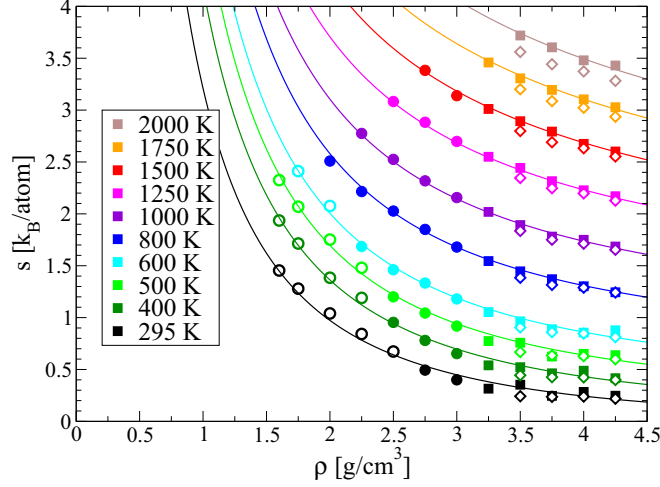
FIG. 5. (Color online) Entropy calculated from the MD simulations via Eq. (4) for different isotherms. For ice VII the structural entropy from Eq. (10) was added. The open circles represent ice VII, the solid circles indicate ice VII*, and the squares show ice X. The open diamonds are results from the phonon calculations for ice X. Thin lines with the same colors as the symbols show the results from the fit to Eq. (13).

mode in $S(\nu)$ approach zero, rendering the integrand in Eq. (4) finite for all frequencies.

Several isotherms of the entropy are displayed in Fig. 5. The entropy increases systematically with the temperature and decreases with the density. The statistical uncertainty is lower at higher temperatures due to the larger anharmonicity in the vibrations. This corresponds to a higher collision rate among the phonons and thus a more effective sampling of the phase space during a simulation. This statistical effect is especially visible in the data points for ice X, which remains relatively harmonic up to almost 1000 K. Therefore, we did not use the entropies from the MD below 800 K in the ice X region but used the results from the phonon calculations down to 5 K when performing the fitting procedure. The systematically growing deviation between the phonon entropy and the MD entropy at high temperature can be explained by anharmonic effects.

Designing a physically meaningful analytic expression to fit the entropy of such a complex solid is a challenging task. We choose the following ansatz for the thermal part of the free energy:

$$f_t(\varrho,T) = \sum_{ik} \alpha_{ik} T [3\ln(1 - e^{-T_i/T}) - D(T_i/T)]\varrho^{k/k_0}$$
$$+ \sum_{jk} \gamma_{jk} T \ln(1 - e^{-T_j/T})\varrho^{k/k_0}. \quad (11)$$

This expression is a superposition of terms with temperature dependences taken from standard Debye and Einstein models [49,80,81], each of which has a different characteristic vibrational temperature. It contains a polynomial density dependence. The Debye function is defined as

$$D(z) = \frac{3}{z^3} \int_0^z dx \frac{x^3}{e^x - 1}. \quad (12)$$

The corresponding expression for the entropy is gained by differentiation:

$$s(\varrho,T) = -\left(\frac{\partial f_t}{\partial T}\right)_\varrho$$
$$= \sum_{ik} \alpha_{ik}[4D(T_i/T) - 3\ln(1 - e^{-T_i/T})]\varrho^{k/k_0}$$
$$+ \sum_{jk} \gamma_{jk}\left[\frac{T_j}{T}\frac{1}{e^{T_j/T} - 1} - \ln(1 - e^{-T_j/T})\right]\varrho^{k/k_0}. \quad (13)$$

It contains parameters identical to those in Eq. (11). The parameter optimization is performed semiautomatically as follows: as a first step, a reasonable set of characteristic frequencies needs to be obtained. This is accomplished by examining the entropy from a phonon calculation for ice X along an isochore. Geometric sequences of the following form are chosen for the characteristic temperatures:

$$T_i = T_D a_D^i, \qquad T_j = T_E a_E^j, \quad (14)$$

where T_D and T_E are the Debye and Einstein base temperatures and $a_D = a_E = 2$. It turns out that an excellent fit to each of the entropy isochores of ice X can be made with one Debye temperature of 700 K and Einstein temperatures of 1000, 2000, 4000, and 8000 K, and we thus define $T_D = 700$ K and $T_E = 1000$ K. The density dependence of the entropy is well described by combined powers of $\varrho^{-2/3}$, ϱ^{-1}, and $\varrho^{-4/3}$ over the entire density range, so that we set $k_0 = 3$.

Having preoptimized the nonlinear fit coefficients manually, we then determine the coefficients α_{ik} and γ_{jk} with a linear regression. The respective numerical values are given in Table II.

There is no need to perform an automatic reoptimization of the nonlinear parameters in Eq. (11). Importantly, the functional form is capable of describing deviations from the harmonic behavior on its own, simply due to the automatic

TABLE II. Coefficients α_{ik} and γ_{jk} used in Eqs. (11) and (13). All units are chosen in a way that entering the temperature in K and the density in g/cm^3 leads to results for f_t in kJ/g.

Coefficient	Value
$\alpha_{0,-4}$	6.869192×10^{-3}
$\alpha_{0,-3}$	-3.919234×10^{-3}
$\alpha_{0,-2}$	6.790631×10^{-5}
$\gamma_{0,-4}$	-2.604037×10^{-2}
$\gamma_{0,-3}$	2.104060×10^{-2}
$\gamma_{0,-2}$	-1.515928×10^{-3}
$\gamma_{1,-4}$	6.721305×10^{-2}
$\gamma_{1,-3}$	-1.158057×10^{-1}
$\gamma_{1,-2}$	5.234025×10^{-2}
$\gamma_{2,-4}$	-1.178112×10^{-1}
$\gamma_{2,-3}$	1.754266×10^{-1}
$\gamma_{2,-2}$	-6.213482×10^{-2}
$\gamma_{3,-4}$	1.206828×10^{-1}
$\gamma_{3,-3}$	-1.910820×10^{-1}
$\gamma_{3,-2}$	7.712887×10^{-2}

optimization of the linear parameters α_{ik} and γ_{jk} chosen here. It also maintains a good behavior when extrapolated toward high temperatures. Figure 5 contains the fitted entropies in comparison with the underlying data.

There was, however, one sacrifice made with the ansatz (11); that is, the entropy is exactly zero at $T = 0$ for all densities. Thus, a residual zero-point entropy from proton disorder in ice VII [see Eq. (10)] is not achieved. But since ice VII becomes unstable when cooled to far below room temperature, i.e., it transforms into ice VIII [1], this is not a serious drawback in practice. The magnitude of the residual entropy is relatively small. Its effective absorption into the heat capacity at very low temperature will not be harmful in practical applications for the thermodynamic potential constructed here.

Last, we made several additional MD simulations with the LDA but did not find an effect on the entropies within the statistical accuracy. The XC functional thus does not significantly influence the thermal part $f_t(\varrho,T)$.

C. Nuclear ground-state energy

The physical origin of the remaining term, $u_n(\varrho)$, is the quantum-mechanical zero-point motion of the nuclei. Direct calculation, e.g., within a phonon treatment, is not possible because the idealized crystal structure of ice VII used here (see Fig. 1) is dynamically unstable for $l_1 < l_2$. We checked that relaxation of the nuclear coordinates leads to a slight proton migration away from the positions on the space diagonal [14] of the unit cell. However, an effective $u_n(\varrho)$ can be determined with the help of the internal energy of the MD simulations, most importantly, by including the vibrational quantum corrections.

In doing so, we subtract the previously constructed fit functions for the electronic ground-state energy $u_e(\varrho)$ as well as the term containing all temperature-dependent contributions, $u_t(\varrho,T) = f_t(\varrho,T) + Ts(\varrho,T)$, from the respective MD simulation data for $u_{MD}(\varrho,T) + u_{vc}(\varrho,T)$. This should yield a temperature-independent set of data, provided that the construction of the thermal part via the entropy was done with sufficient accuracy. The residual data should also resemble the qualitative behavior of the quantum correction term $u_{vc}(\varrho,T)$ when extrapolated to $T = 0$. Both conditions are fulfilled well, and the results are shown as small symbols in Fig. 3 together with the fit, which takes the following functional form:

$$u_n(\varrho) = b_0 + b_1\varrho + b_2\varrho^2 + b_3 \exp(-b_4\varrho^{10}). \quad (15)$$

The respective coefficients are given in Table III.

TABLE III. Coefficients used in Eq. (15). All units are chosen in a way that entering the density in g/cm^3 leads to results for u_n in kJ/g.

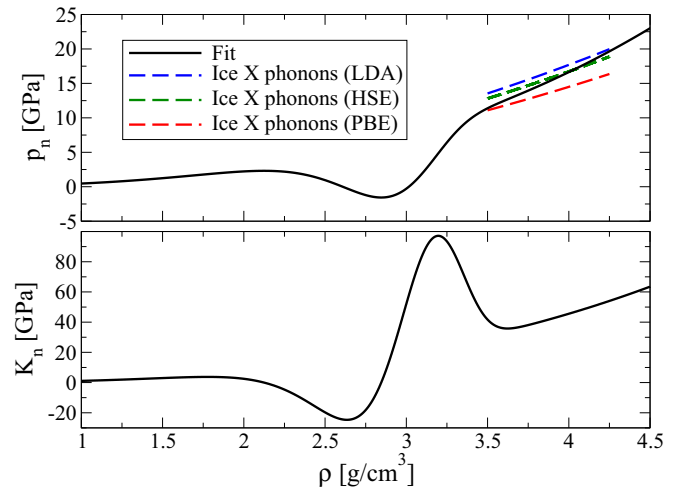| Coefficient	Value
b_0	2.08
b_1	0.272
b_2	0.096
b_3	0.788
b_4	2.54×10^{-5}

FIG. 6. (Color online) Nuclear ground-state pressure from Eq. (15) compared with phonon calculations for ice X made with different XC functionals (top). The corresponding nuclear ground-state bulk modulus (bottom).

Of particular interest is the corresponding pressure term, $p_n(\varrho) = \varrho^2(\partial u_n/\partial\varrho)$, which is displayed in Fig. 6. It shows three regions with either a positive or negative sign. A positive $p_n(\varrho)$ results from a rising $u_n(\varrho)$ and is thus a consequence of a general increase of vibrational frequencies with the density. This is observed for low densities (ice VII region), and it is especially pronounced in the density region associated with the crystalline ice X phase. The negative sign in the intermediate region stems from the effective decrease of vibrational frequencies that happens in ice VII*, which was already presented in Sec. III B. The strong increase in the nuclear quantum pressure above 3 g/cm^3 is responsible for a noticeable stiffening of the total pressure in the ice X region, an effect which was predicted much earlier [7,30].

The transition from ice VII* to ice X is also accompanied by a local maximum in the nuclear bulk modulus $K_n(\varrho) = \varrho(\partial p_n/\partial\varrho)$ (see bottom panel of Fig. 6). This effect has been qualitatively discussed by Sugimura *et al.* [23], who used a simple model of proton motion in a square-well potential to interpret their experimental findings.

In the case of ice X we have the possibility to compare $u_n(\varrho)$ with the results from the phonon calculations, which we performed for different XC functionals. The phonon ground-state energies can be fitted very well with linear functions of the density. The respective pressures are included in Fig. 6. We observe a good concordance of these results with the $p_n(\varrho)$ curve. Note that an ideal agreement between the PBE phonon curve and $p_n(\varrho)$ cannot be expected to occur because the latter is only an effective ground-state quantity, derived using various mathematical procedures. For example, it is directly influenced by the electronic ground-state energy function $u_e(\varrho)$ at all densities and may even compensate a potential inaccuracy of the latter [82].

The effect of the XC functional on the ground-state energy is estimated by examining the pressures from the phonon calculations for ice X, which are plotted in Fig. 6. The overall magnitude of the phonon pressure is roughly 5% of that

from the electronic ground-state term shown in Fig. 4. The difference between the PBE and LDA results amounts to 3 or 4 GPa, whereas the LDA pressure is higher than that from PBE and also close to the HSE result. There is thus a partial compensation between the deviations when adding $p_n(\varrho)$ to $p_e(\varrho)$. The variation between the XC functionals for $p_n(\varrho)$ amounts to about 1% of the total pressure $p(\varrho)$, which is only a relatively minor source of error. The values from the vdW-optB86b XC functional are virtually on top of the PBE results and are not shown in Fig. 6.

We cannot make a similarly sound comparison for the ice VII and ice VII* regions, but we expect the insight gained from ice X to be transferable to the whole picture. The magnitude of $p_n(\varrho)$ is much smaller in the ice VII and ice VII* regions than it is for ice X. Nevertheless, we conclude that it is important to consider electronic structure and nuclear quantum effects together when evaluating different XC functionals for a ground-state EOS.

D. Assessment of uncertainty and check against DFT-MD data

Here we discuss the numerical accuracy reached with the fitting procedures. It is best characterized by the variation in the residual data obtained to fit the nuclear ground-state energy in the previous section (see Fig. 3). These residual data contain, apart from statistical fluctuations, a partially systematic trend in temperature, but only a few points deviate from the fit $u_n(\varrho)$ by more than 0.1 kJ/g. The main source of the uncertainty can be traced back to the fidelity of the entropy fit, which is based on the smooth free-energy function describing ices VII, VII*, and X combined. This causes a blurring of subtle details in the underlying thermodynamic data, e.g., close to possible second-order transitions between the phases. However, such a disadvantage is highly outweighed by the simplicity of Eqs. (6), (9), (11), and (15), which capture the principal thermodynamic behavior of the ices very well and show good behavior when extrapolated beyond the stability region of the ices. Another source of error is the approximations made when calculating thermodynamic quantities from power spectra [62], although their particular influence is difficult to quantify here.

We compare the internal energy from Eq. (8) with the data from the MD simulations in Fig. 7. It is easily observed that typical changes in energy over temperature differences of order 2000 K are much larger than 0.1 kJ/g.

We cannot make a corresponding comparison for the pressure because we do not have access to the quantum correction term $p_{vc}(\varrho,T)$ from the MD simulations. Calculating that quantity would, for instance, require a density derivative of the power spectra $S(\nu)$.

For additional illustration we show two isochores of the entropy and heat capacity c_v of ice X compared with the phonon and MD data in Fig. 8. The isochoric heat capacity is a sensitive quantity. It is defined as

$$c_v = T \left(\frac{\partial s}{\partial T} \right)_\varrho . \tag{16}$$

At 4 g/cm³ there is almost perfect agreement between the fit and the results of the phonon calculations for low temperatures. A small but noticeable deviation occurs at 3.5 g/cm³ for
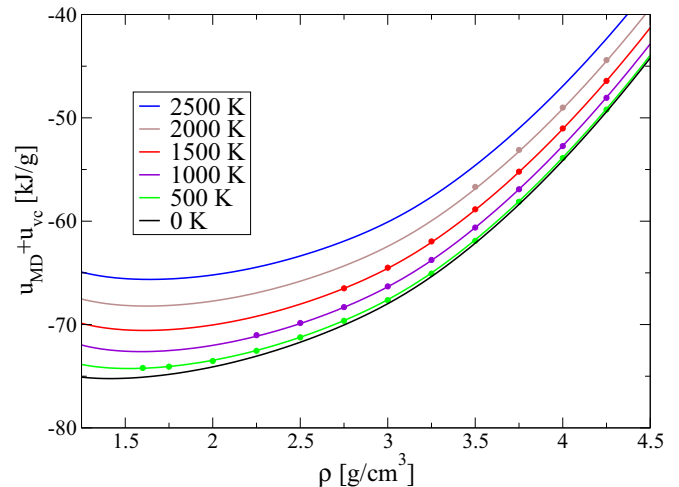

FIG. 7. (Color online) Isotherms of the internal energy data from the MD simulation, $u_{MD}(\varrho,T) + u_{vc}(\varrho,T)$ (circles), compared with the respective results of the fit [Eq. (8); lines].

low temperatures, which is a consequence of the smooth parametrization of the density dependence in the entropy, as was discussed above. The heat capacity from the phonon calculations tends to converge toward the Dulong-Petit limit of $3k_B$/atom at high temperature. Systematic deviations in entropy and heat capacity emerge between the fit [Eq. (13)] and the phonon calculations as the temperature increases. This illustrates the pronounced effect of anharmonicity in the vibrations at high temperature.

V. COMPARISON WITH EXPERIMENTS AND DISCUSSION

Here we make a detailed comparison between pressures $p = \varrho^2 (\partial f/\partial \varrho)_T$ calculated from our free-energy fit [Eq. (6)] and data from diamond-anvil cell experiments.
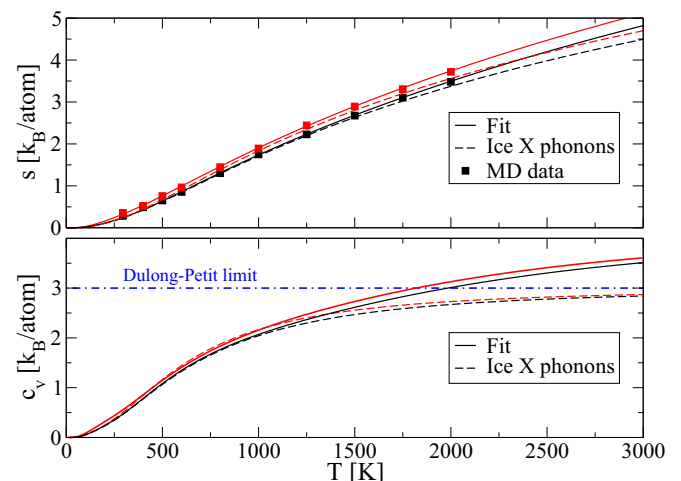

FIG. 8. (Color online) Entropy (top) and heat capacity (bottom) in ice X at 3.5 g/cm³ (red) and 4 g/cm³ (black) calculated from the fit [Eq. (13); solid lines] and from the phonon calculations (dashed lines).
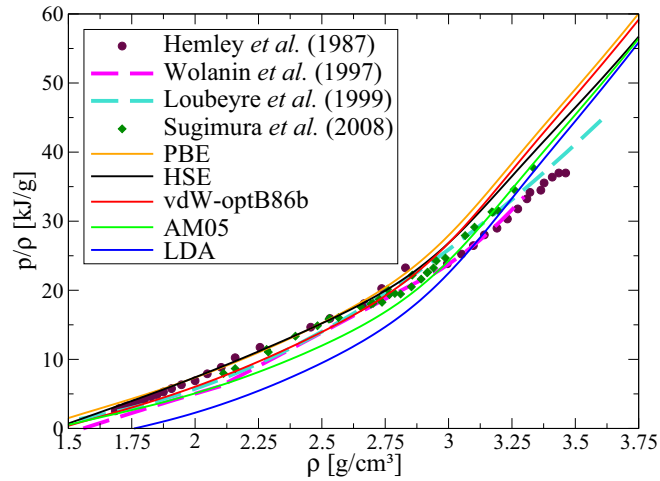
FIG. 9. (Color online) Reduced pressure p/ϱ derived with Eq. (6) using different XC functionals for $u_e(\varrho)$ (see Table I) compared with experiments [8,12,15,23].

A. The pressure-volume relation at room temperature

In Fig. 9 we examine the 295 K isotherm, for which the pressure-density relation was probed up to very high pressures in a variety of experiments [8,12,15,20,23].

The pressures from the fit [Eq. (6)] are calculated using different XC functionals for the electronic ground-state energy $u_e(\varrho)$ (see Table I). Recalling the discussions made in Sec. IV, this term is the major source of uncertainty in our calculations. For densities below 3 g/cm^3 the PBE, HSE, and vdW-optB86b functionals are in good agreement with the various experimental data. The LDA and the AM05 functionals yield too low pressures there, which is in line with typical trends known from DFT benchmark calculations for various substances [73,75–77].

Above 3 g/cm^3, the LDA and AM05 XC functionals are in better agreement with the experiments than the PBE, HSE, or vdW-optB86b XC functionals. The latter three significantly exceed the experimental pressures. However, even the LDA pressure curve is still higher than three of the four experimental data sets [8,12,15,23]. Such an overshooting of the pressure is an extremely rare observation in DFT calculations within the LDA [73,75–77]. The AM05 and HSE functionals are intermediate between the vdW-optB86b functional at low densities and the LDA functional at high densities. Thus, these two XC functionals give a description of the change in electronic structure along the transition from the molecular to the ionic state of ice that is noticeably different from that of LDA, PBE, or vdW-optB86b. The overall best agreement is achieved with the HSE functional.

Considering the significant deviations between the different experiments as well, it would be very beneficial if another accurate measurement of the pressure-density relation in ice X could be performed. Having such significant discrepancies between several individual experimental data sets also makes the application of postprocessing methods for corrections of DFT-MD EOS [83] very difficult. Also, the fitting of experimental data for such a complex solid may require using a more refined parametric EOS [84] than the simple Vinet formula, even when the EOS is split into multiple sections [12].
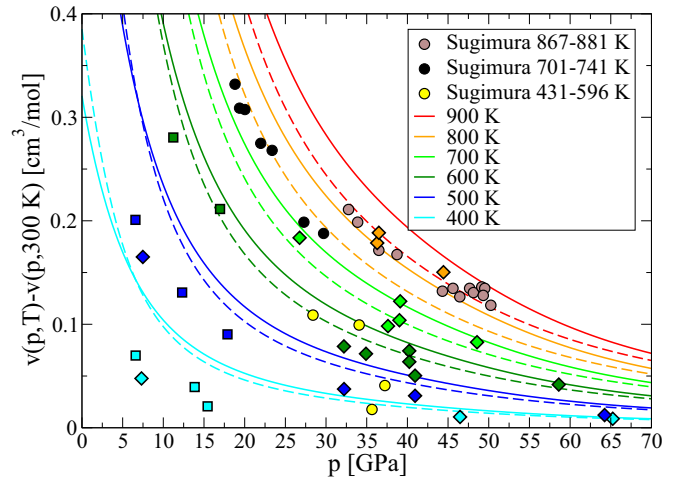

FIG. 10. (Color online) Differences in the specific volume derived from Eq. (6) using different XC functionals for $u_e(\varrho)$ from Table I. Solid lines were generated with the HSE hybrid functional, and dashed lines are results from the vdW-optB86b XC functional. Squares show the measurements of Fei *et al.* [9], and the diamonds represent the experimental results of Frank *et al.* [20]. The data from Sugimura *et al.* [26] are indicated by circles, and their temperatures are given in the legend.

B. Volume expansion at elevated temperatures

To validate the temperature-dependent part of our EOS with measurements, we plot the difference in volume between several isotherms and the 300 K reference isotherm versus the pressure in Fig. 10. This is a commonly used representation that allows us to examine the thermal expansion at constant pressure [9,20,26]. However, it is still sensitive to the XC functional. A perfect reproduction of experimental data cannot be expected, unless the reference isotherm from theory is very close to those from the experiments.

The experimental room-temperature isotherm [9,20,23,26] is reproduced well with the HSE XC functional in the pressure region of interest here. Therefore, it is most meaningful to compare the volume expansion with the theoretical curves from that particular XC functional. Agreement between the calculated curves and the measurements is generally achieved within the typical experimental uncertainties of 0.02 to 0.05 cm^3/mol. Such a deviation translates into temperature differences of 50 K or less. We thus conclude that the derivation of the thermal part $f_t(\varrho,T)$ from the calculated entropy (see Sec. IV B) has been successful.

VI. CONCLUSION AND FINAL RECOMMENDATION

In summary, we have constructed a smooth thermodynamic potential $f(\varrho,T)$ for ices VII, VII*, and X that is highly accurate, easy to apply, and valid in the entire stability region of the three ice phases. Expression (6) is composed of three individual terms, which are separately described by Eqs. (9), (11), and (15). For standard applications we recommend using the electronic ground-state parametrization derived with the HSE XC functional (second row in Table I) [85]. This recommendation is based mainly on the generally good reproduction of experimental EOS data, especially for densities below

3 g/cm^3. Resolving the residual deviation between the theory and the experimental pressures in the denser ice X will require further experimental and theoretical investigation. For example, the employment of computational approaches beyond DFT, such as quantum Monte Carlo methods [74,86,87], might give additional insight here. Apart from that, the procedure developed here for the construction of a free-energy function from DFT-MD simulations is directly transferable to other materials whose complexity is comparable to or even higher than that of ices VII and X.

APPENDIX: ON THERMODYNAMIC QUANTITIES DERIVED FROM FREQUENCY SPECTRA

Here we briefly discuss some important aspects and limitations of the method described by Berens *et al.* [62].

First, all weighting functions are based on the harmonic oscillator model. Consequently, there is no guarantee that anharmonic effects are fully accounted for. Although anharmonicity is included in the spectra $S(\nu,\varrho,T)$, the use of harmonic weighting functions implies that anharmonicity enters the calculated physical quantities only in the form of effective harmonic contributions. In the case of quantum-correction quantities like $u_{vc}(\varrho,T)$, the resulting error is very small because all quantum corrections naturally decrease to zero at high temperature, which is where the anharmonicity is significant. For complete state quantities like $s_{\rm vib}(\varrho,T)$, it is very hard to estimate up to which degree the anharmonicity is captured at high temperature without having an exactly known and representative reference system.

Second, a set of thermodynamic quantities (partition function, free energy, entropy, etc.) calculated with $S(\nu,\varrho,T)$ and corresponding weighting functions like Eqs. (3.39)–(3.43) in Ref. [62] does not form a thermodynamically consistent EOS. The reason is that the spectra $S(\nu,\varrho,T)$ depend on density and temperature. Formal thermodynamic consistency can be achieved only by including additional terms with partial derivatives of the spectra $S(\nu,\varrho,T)$ in the weighting functions. However, the actual variation of the spectra with temperature is small enough that the degree of inconsistency between $s_{\rm vib}(\varrho,T)$ and $u_{MD}(\varrho,T) + u_{vc}(\varrho,T)$ is harmless in this work.

[1] V. F. Petrenko and R. W. Whitworth, *Physics of Ice* (Oxford University Press, Oxford, 1999).

[2] R. Fu, R. J. O'Connell, and D. D. Sasselov, Astrophys. J. **708**, 1326 (2010).

[3] L. Zeng and D. Sasselov, Astrophys. J. **784**, 96 (2014).

[4] A. Polian and M. Grimsditch, Phys. Rev. Lett. **52**, 1312 (1984).

[5] K. R. Hirsch and W. B. Holzapfel, Phys. Lett. A **101**, 142 (1984).

[6] W. F. Kuhs, J. L. Finney, C. Vettier, and D. V. Bliss, J. Chem. Phys. **81**, 3612 (1984).

[7] K. R. Hirsch and W. B. Holzapfel, J. Chem. Phys. **84**, 2771 (1986).

[8] R. J. Hemley, A. P. Jephcoat, H. K. Mao, C. S. Zha, L. W. Finger, and D. E. Cox, Nature (London) **330**, 737 (1987).

[9] Y. Fei, H.-k. Mao, and R. J. Hemley, J. Chem. Phys. **99**, 5369 (1993).

[10] A. F. Goncharov, V. V. Struzhkin, M. S. Somayazulu, R. J. Hemley, and H. K. Mao, Science **273**, 218 (1996).

[11] P. Pruzan, E. Wolanin, M. Gauthier, J. C. Chervin, B. Canny, D. Hausermann, and M. Hanfland, J. Phys. Chem. B **101**, 6230 (1997).

[12] E. Wolanin, P. Pruzan, J. C. Chervin, B. Canny, M. Gauthier, D. Häusermann, and M. Hanfland, Phys. Rev. B **56**, 5781 (1997).

[13] V. V. Struzhkin, A. F. Goncharov, R. J. Hemley, and H.-k. Mao, Phys. Rev. Lett. **78**, 4446 (1997).

[14] R. J. Nelmes, J. S. Loveday, W. G. Marshall, G. Hamel, J. M. Besson, and S. Klotz, Phys. Rev. Lett. **81**, 2719 (1998).

[15] P. Loubeyre, R. LeToullec, E. Wolanin, M. Hanfland, and D. Hausermann, Nature (London) **397**, 503 (1999).

[16] A. F. Goncharov, V. V. Struzhkin, H.-k. Mao, and R. J. Hemley, Phys. Rev. Lett. **83**, 1998 (1999).

[17] E. Katoh, M. Song, H. Yamawaki, H. Fujihisa, M. Sakashita, and K. Aoki, Phys. Rev. B **62**, 2976 (2000).

[18] P. Pruzan, J. C. Chervin, E. Wolanin, B. Canny, M. Gauthier, and M. Hanfland, J. Raman Spectrosc. **34**, 591 (2003).

[19] M. Song, H. Yamawaki, H. Fujihisa, M. Sakashita, and K. Aoki, Phys. Rev. B **68**, 014106 (2003).

[20] M. R. Frank, Y. Fei, and J. Hu, Geochim. Cosmochim. Acta **68**, 2781 (2004).

[21] A. F. Goncharov, N. Goldman, L. E. Fried, J. C. Crowhurst, I.-F. W. Kuo, C. J. Mundy, and J. M. Zaug, Phys. Rev. Lett. **94**, 125508 (2005).

[22] J. F. Lin, E. Gregoryanz, V. V. Struzhkin, M. Somayazulu, H. K. Mao, and R. J. Hemley, Geophys. Res. Lett. **32**, L11306 (2005).

[23] E. Sugimura, T. Iitaka, K. Hirose, K. Kawamura, N. Sata, and Y. Ohishi, Phys. Rev. B **77**, 214103 (2008).

[24] M. Somayazulu, J. Shu, C.-s. Zha, A. F. Goncharov, O. Tschauner, H.-k. Mao, and R. J. Hemley, J. Chem. Phys. **128**, 064510 (2008).

[25] A. F. Goncharov, C. Sanloup, N. Goldman, J. C. Crowhurst, S. Bastea, W. M. Howard, L. E. Fried, N. Guignot, M. Mezouar, and Y. Meng, J. Chem. Phys. **130**, 124514 (2009).

[26] E. Sugimura, T. Komabayashi, K. Hirose, N. Sata, Y. Ohishi, and L. S. Dubrovinsky, Phys. Rev. B **82**, 134103 (2010).

[27] M. Ahart, M. Somayazulu, S. A. Gramsch, R. Boehler, H.-k. Mao, and R. J. Hemley, J. Chem. Phys. **134**, 124517 (2011).

[28] M. Guthrie, R. Boehler, C. A. Tulk, J. J. Molaison, A. M. dos Santos, K. Lia, and R. J. Hemley, Proc. Natl. Acad. Sci. USA **110**, 10552 (2013).

[29] N. Noguchi, K. Komatsu, A. Shinozaki, K. Shinoda, and H. Kagi, Spectrochim. Acta A **133**, 509 (2014).

[30] W. B. Holzapfel, J. Chem. Phys. **56**, 712 (1972).

[31] K. S. Schweizer and F. H. Stillinger, J. Chem. Phys. **80**, 1230 (1984).

[32] M. Bernasconi, P. L. Silvestrelli, and M. Parrinello, Phys. Rev. Lett. **81**, 1235 (1998).

[33] M. Benoit, D. Marx, and M. Parrinello, Nature (London) **392**, 258 (1998).

[34] M. Benoit, A. H. Romero, and D. Marx, Phys. Rev. Lett. **89**, 145501 (2002).

[35] E. Schwegler, M. Sharma, F. Gygi, and G. Galli, Proc. Natl. Acad. Sci, USA **105**, 14779 (2008).

[36] R. Caracas, Phys. Rev. Lett. **101**, 085502 (2008).

[37] J. A. Morrone, L. Lin, and R. Car, J. Chem. Phys. **130**, 204511 (2009).

[38] Y. Bronstein, P. Depondt, F. Finocchi, and A. M. Saitta, Phys. Rev. B **89**, 214101 (2014).

[39] Although very slight displacements of protons off the space diagonal have been found experimentally [6, 14], this picture of ices VII and X captures their key differences well enough for us to interpret their basic thermodynamic properties.

[40] P. Hohenberg and W. Kohn, Phys. Rev. **136**, B864 (1964).

[41] W. Kohn and L. J. Sham, Phys. Rev. **140**, A1133 (1965).

[42] N. D. Mermin, Phys. Rev. **137**, A1441 (1965).

[43] G. Kresse and J. Hafner, Phys. Rev. B **47**, 558 (1993).

[44] G. Kresse and J. Hafner, Phys. Rev. B **48**, 13115 (1993).

[45] G. Kresse and J. Furthmüller, Phys. Rev. B **54**, 11169 (1996).

[46] P. E. Blöchl, Phys. Rev. B **50**, 17953 (1994).

[47] G. Kresse and D. Joubert, Phys. Rev. B **59**, 1758 (1999).

[48] J. P. Perdew, K. Burke, and M. Ernzerhof, Phys. Rev. Lett. **77**, 3865 (1996).

[49] D. C. Wallace, *Statistical Physics of Crystals and Liquids* (World Scientific, Singapore, 2002).

[50] M. J. Gillan, D. Alfe, J. Brodholt, L. Vocadlo, and G. D. Price, Rep. Prog. Phys. **69**, 2365 (2006).

[51] A. Togo, F. Oba, and I. Tanaka, Phys. Rev. B **78**, 134106 (2008).

[52] S. Nosé, J. Chem. Phys. **81**, 511 (1984).

[53] A. E. Mattsson, P. A. Schultz, M. P. Desjarlais, T. R. Mattsson, and K. Leung, Modell. Simul. Mater. Sci. Eng. **13**, R1 (2005).

[54] M. French, T. R. Mattsson, N. Nettelmann, and R. Redmer, Phys. Rev. B **79**, 054107 (2009).

[55] M. French and R. Redmer, J. Phys. Condens. Matter **21**, 375101 (2009).

[56] M. French, T. R. Mattsson, and R. Redmer, Phys. Rev. B **82**, 174108 (2010).

[57] R. Redmer, T. R. Mattsson, N. Nettelmann, and M. French, Icarus **211**, 798 (2011).

[58] M. French and R. Redmer, Phys. Plasmas **18**, 043301 (2011).

[59] M. French, S. Hamel, and R. Redmer, Phys. Rev. Lett. **107**, 185901 (2011).

[60] M. Schöttler, R. Redmer, and M. French, Contrib. Plasma Phys. **53**, 336 (2013).

[61] H. J. Monkhorst and J. D. Pack, Phys. Rev. B **13**, 5188 (1976).

[62] P. H. Berens, D. H. J. Mackay, G. M. White, and K. R. Wilson, J. Chem. Phys. **79**, 2375 (1983).

[63] M. Bethkenhagen, M. French, and R. Redmer, J. Chem. Phys. **138**, 234504 (2013).

[64] T. Qi and E. J. Reed, J. Phys. Chem. A **116**, 10451 (2012).

[65] C. Cavazzoni, G. L. Chiarotti, S. Scandolo, E. Tosatti, M. Bernasconi, and M. Parrinello, Science **283**, 44 (1999).

[66] M. Benoit, M. Bernasconi, P. Focher, and M. Parrinello, Phys. Rev. Lett. **76**, 2934 (1996).

[67] In contrast, the transitions between the ices and either the fluid or the superionic phase are accompanied by a pronounced discontinuity in pressure and internal energy [54].

[68] D. M. Ceperley and B. J. Alder, Phys. Rev. Lett. **45**, 566 (1980).

[69] J. P. Perdew and A. Zunger, Phys. Rev. B **23**, 5048 (1981).

[70] R. Armiento and A. E. Mattsson, Phys. Rev. B **72**, 085108 (2005).

[71] J. Heyd, G. E. Scuseria, and M. Ernzerhof, J. Chem. Phys. **118**, 8207 (2003).

[72] J. Heyd, G. E. Scuseria, and M. Ernzerhof, J. Chem. Phys. **124**, 219906 (2006).

[73] J. Klimeš, D. R. Bowler, and A. Michaelides, Phys. Rev. B **83**, 195131 (2011).

[74] L. Shulenburger and T. R. Mattsson, Phys. Rev. B **88**, 245117 (2013).

[75] P. Haas, F. Tran, and P. Blaha, Phys. Rev. B **79**, 085104 (2009).

[76] G. I. Csonka, J. P. Perdew, A. Ruzsinszky, P. H. T. Philipsen, S. Lebègue, J. Paier, O. A. Vydrov, and J. G. Ángyán, Phys. Rev. B **79**, 155107 (2009).

[77] A. E. Mattsson, R. Armiento, J. Paier, G. Kresse, J. M. Wills, and T. R. Mattsson, J. Chem. Phys. **128**, 084714 (2008).

[78] L. Schimka, J. Harl, and G. Kresse, J. Chem. Phys. **134**, 024116 (2011).

[79] L. Pauling, J. Am. Chem. Soc. **57**, 2680 (1935).

[80] A. Einstein, Ann. Phys. (Berlin, Germany) **327**, 180 (1906).

[81] P. Debye, Ann. Phys. (Berlin, Germany) **344**, 789 (1912).

[82] In principle, we could have omitted Sec. VI A and merged all ground-state terms into a single function instead. However, the insightful discussions concerning the influence of the XC functional would not have been possible that way.

[83] M. French and T. R. Mattsson, J. Appl. Phys. **116**, 013510 (2014).

[84] W. B. Holzapfel, Z. Kristallogr. **216**, 473 (2001).

[85] The inconsistency (not considering an arbitrary constant offset in the internal energy) introduced by replacing the XC functional exclusively in $u_e(\varrho)$ is small because the remaining two terms, $u_n(\varrho)$ and $f_t(\varrho,T)$, are only weakly dependent on the XC functional.

[86] B. Santra, J. Klimeš, D. Alfè, A. Tkatchenko, B. Slater, A. Michaelides, R. Car, and M. Scheffler, Phys. Rev. Lett. **107**, 185701 (2011).

[87] M. A. Morales, J. R. Gergely, J. McMinis, J. M. McMahon, J. Kim, and D. M. Ceperley, J. Chem. Theory Comput. **10**, 2355 (2014).